

Regularization of Inverse Problems: Deep Equilibrium Models versus Bilevel Learning

Danilo Riccio

Matthias J. Ehrhardt

Martin Benning

June 28, 2022

Abstract

Variational regularization methods are commonly used to approximate solutions of inverse problems. In recent years, model-based variational regularization methods have often been replaced with data-driven ones such as the fields-of-expert model [29]. Training the parameters of such data-driven methods can be formulated as a bilevel optimization problem. In this paper, we compare the framework of bilevel learning for the training of data-driven variational regularization models with the novel framework of deep equilibrium models [3] that has recently been introduced in the context of inverse problems [12]. We show that computing the lower-level optimization problem within the bilevel formulation with a fixed point iteration is a special case of the deep equilibrium framework. We compare both approaches computationally, with a variety of numerical examples for the inverse problems of denoising, inpainting and deconvolution.

1 Introduction

In inverse problems, a desired quantity can only be recovered indirectly from measurements through the inversion of a so-called forward operator. Inverse problems are found in many diverse research areas like medical and industrial imaging, signal and image processing, computer vision, or geophysics, with various applications utilizing inverse problems such as Computerized Tomography, Magnetic Resonance Imaging, or Transmission Electron Tomography, see e.g. [25, 30] and references therein. For the majority of relevant inverse problems, an inverse of the forward operator is discontinuous and usually not unique. If we focus on inverse problems with linear forward operators in finite dimensions, an inverse (if it exists) is no longer discontinuous, but can still be very sensitive to small variations in the argument if the condition number of the linear forward operator (which is then a matrix) is large.

Regularizations are parameterized operators that approximate inverses of forward operators in a continuous fashion [32, 11, 6]. Variational regularizations [30] are a special class of regularizations and usually assign the solution of a convex optimization problem to the operator input. Regularizations are equipped with hyper-parameters that are usually referred to as regularization parameters, and these regularization parameters have to be chosen dependent on the data error to guarantee that a regularization converges to a (generalized) inverse when the error goes to zero.

A heuristic regularization parameter choice strategy that has been popularized in the past decade is the identification of optimal regularization parameters in a data-driven way with bilevel optimization [28, 19, 26, 27, 10, 9]. In a bilevel optimization problem, an upper-level objective that is constrained by a lower-level objective is optimized. In the context of variational

regularization parameter estimation, one can for example minimize an empirical risk between the regularization operator outputs and a set of desired outputs as the upper-level optimization problem, subject to the lower-level optimization problem that the regularization operator outputs have to solve the optimization problem associated with the variational regularization.

In a development parallel to the use of bilevel optimization for the estimation of regularization parameters, more and more inverse problem solutions have been approximated with operators stemming from deep neural networks, with great empirical success [13, 14, 37, 1, 2, 18, 35, 17]. A recent development is the application of so-called deep equilibrium models [3] in the context of inverse problems [12]. Deep equilibrium models are deep learning frameworks where a neural network is trained such that its fixed point approximates some ground truth solution.

None of the aforementioned papers have investigated the obvious link between deep equilibrium models and bilevel optimization. Our contributions are the framing of bilevel optimization problems with strongly convex lower-level problem as deep equilibrium models, and an extensive empirical comparison of deep equilibrium models and bilevel optimization for three inverse problems.

The paper is organized as follows. In Section 2, we give a brief overview of the concepts of inverse problems, regularizations, bilevel optimization and deep equilibrium models. In Section 3, we choose different bilevel and deep equilibrium models for comparison and explain their architectures and other design choices. In Section 3.3, we present the three inverse problems denoising, inpainting and deblurring that we use for the numerical deep equilibrium vs bilevel optimization comparison in Section 4. We then wrap up with conclusions and give an outlook for open research questions in Section 5.

2 Deep equilibrium models and bilevel learning

In this section we briefly recall the fundamentals of inverse problems and variational regularization. Subsequently, we describe the concepts of bilevel optimization and deep equilibrium models in this context, and highlight how they are linked mathematically. We conclude this section with a comment on why learning fixed points in a naïve way does not work.

2.1 Inverse problems

Many practical applications such as Computed Tomography (CT) and Magnetic Resonance Imaging (MRI) require the reconstruction of quantities from indirect measurements. This task can be modeled as an inverse problem

$$Ku = f, \tag{1}$$

where the goal is to retrieve an unknown quantity u given the operator K and the *ideal* measured data f , with $u \in \mathbb{R}^n, f \in \mathbb{R}^m, K \in \mathbb{R}^{m \times n}$. In this paper, we limit our analysis to linear and finite dimensional operators K , so that we can think of K as a $m \times n$ matrix.

If the operator K is invertible, the unique solution of (1) is $u = K^{-1}f$. In case the operator K is not invertible, the Moore–Penrose inverse K^+ can be used to approximate the inverse instead. The Moore–Penrose inverse is the minimum norm solution of the normal equation $K^\top Ku = K^\top f$, which means that it minimizes the least squares function $J(u) = \frac{1}{2}\|Ku - f\|^2$,

where $\|\cdot\|$ is the Euclidean norm, with minimal Euclidean norm $\|u\|$. By using the Moore–Penrose inverse to solve (1) for u , we solve

$$\bar{u} = K^+ f. \quad (2)$$

In most applications, this problem is usually ill-conditioned. In other words, as soon as we consider the presence of noise affecting the measurement, the worst-case error between retrieved data and desired data is strongly amplified. In this paper we will consider any measurement error to be additive, i.e

$$Ku + \delta = f^\delta, \quad (3)$$

$\delta, f^\delta \in \mathbb{R}^n$, where subscript δ is used to remind that the measured data f^δ is affected by (additive) noise.

To avoid getting an ill-conditioned matrix like in (2), a standard procedure known as *variational regularization* is to define a new cost function J_R by adding a regularizer \mathcal{R} to the cost function J , i.e.

$$J_R(u) = \lambda J(u) + \mathcal{R}(u), \quad (4)$$

where J is a proper, convex and continuously differentiable function, \mathcal{R} is a proper, convex and lower semi-continuous function, and $\lambda > 0$ is the so-called regularization parameter that balances the influence of the data term J and the regularizer \mathcal{R} . One of the most famous examples in the literature is the Tikhonov regularizer $\mathcal{R}(u) = \frac{1}{2}\|u\|^2$ (cf. [33]). For example, Tikhonov regularization with the least squares cost function in (4) leads to

$$u_\lambda = (\lambda K^\top K + I_n)^{-1} K^\top f^\delta, \quad (5)$$

where $I_n \in \mathbb{R}^{n \times n}$ is the identity matrix.

More recently, model-based regularizers such as the Tikhonov have been replaced by data-driven regularizers of the form $\mathcal{R}_\Psi(x)$, where subscript Ψ indicates that $\mathcal{R}_\Psi : \mathbb{R}^n \rightarrow \mathbb{R} \cup \{\infty\}$ is a parameterized function with parameters $\Psi \in \mathbb{R}^p$. Examples for such data-driven variational regularizations are Markov Random Field priors like the fields-of-expert regularizer [29], which in combination with (4) was popularized for approximating inverse problems solutions in [7]:

$$u_{\lambda, \Psi} \in \arg \min_{u \in \mathbb{R}^n} \left\{ \frac{\lambda}{2} \|Ku - f^\delta\|^2 + \sum_{i=1}^r \phi_i(A_i u) \right\}. \quad (6)$$

Here $\{\phi_i\}_{i=1}^r$ are proper, convex and lower semi-continuous functions and the parameters are $\Psi = \{A_i\}_{i=1}^r$. Optimal parameters Ψ can be found by training the model for given pairs (u, f^δ) with different techniques. In this paper we compare two of them, namely *bilevel learning* and *deep equilibrium models*.

2.2 Deep equilibrium models

Deep equilibrium models [3] are deep neural networks that have fixed points, and those fixed points are trained to match data samples from a training data set. Suppose we denote by $G(u, \Psi) : \mathbb{R}^n \times \mathbb{R}^p \rightarrow \mathbb{R}^n$ our deep neural network with parameters $\Psi \in \mathbb{R}^p$, then training a deep equilibrium model can be formulated as the constrained optimization problem

$$\min_{\Psi} J(u^*) \quad \text{subject to} \quad u^* = G(u^*, \Psi). \quad (7)$$

We now want to re-formulate (7) with the help of a Lagrange multiplier μ^* to the saddle-point problem $\min_{u^*, \Psi} \max_{\mu^*} \mathcal{L}(u^*, \Psi, \mu^*)$ with

$$\mathcal{L}(u^*, \Psi, \mu^*) = J(u^*) + \langle \mu^*, u^* - G(u^*, \Psi) \rangle, \quad (8)$$

where $\langle \cdot, \cdot \rangle$ denotes the inner product. Computing the optimality system of (8), i.e. computing the partial derivatives of \mathcal{L} with respect to the individual arguments and setting them to zero, yields the nonlinear system of equations

$$u^* = G(u^*, \Psi), \quad (9a)$$

$$0 = \nabla J(u^*) + \left(I - (\partial_{u^*} G(u^*, \Psi))^\top \right) \mu^*, \quad (9b)$$

$$0 = \partial_\Psi G(u^*, \Psi)^\top \mu^*, \quad (9c)$$

where $\partial_{u^*} G(u^*, \Psi)$ and $\partial_\Psi G(u^*, \Psi)$ denote the Jacobi matrices of G with respect to u^* and Ψ respectively. Note that in order to compute a solution u^* of (9a) we are required to solve a fixed point problem and further require that such a fixed point exists. In order to compute a solution μ^* to (9b), we need to solve the linear system $\mu^* = - \left(I - (\partial_{u^*} G(u^*, \Psi))^\top \right)^{-1} \nabla J(u^*)$. In [3] it was proposed to also formulate this problem as a fixed point problem, i.e. we aim to find μ^* that satisfies

$$\mu^* = (\partial_{u^*} G(u^*, \Psi))^\top \mu^* - \nabla J(u^*).$$

It is important to emphasize that, as for the fixed point u^* , we obviously require existence of μ^* in order to be able to compute it. Assuming that we can compute both u^* and μ^* , we can then approximate the gradient of \mathcal{L} with respect to the network parameters Ψ , for instance with a gradient-based iterative algorithm like gradient descent,

$$\Psi_{k+1} = \Psi_k - \tau \partial_\Psi G(u_k^*, \Psi_k)^\top \mu_k^*,$$

where $\{\Psi_k\}_{k=1}^\infty$, $\{u_k^*\}_{k=1}^\infty$ and $\{\mu_k^*\}_{k=1}^\infty$ are sequences to approximate Ψ , u^* and μ^* , and where every u_k^* satisfies $u_k^* = G(u_k^*, \Psi_k)$, while every μ_k^* satisfies $\mu_k^* = (\partial_{u^*} G(u_k^*, \Psi_k))^\top \mu_k^* - \nabla J(u_k^*)$. Here, the parameter τ is a positive step-size parameter that controls the length of the step in the direction of the negative gradient. In practice, any first-order optimization method other than gradient descent can also be used to find optimal parameters Ψ .

In the context of inverse problems of the form (1), we can construct many meaningful deep equilibrium models. In [12], one of the methods of consideration is a so-called DeProx-type method, where a neural network is composed with a gradient descent step on the mean-squared error of the forward model output and the measurement data (which in this context is also known as a step of Landweber regularization), i.e.

$$u^{k+1} = \mathcal{N}_\Psi \left(u^k - \tau \lambda K^\top (K u^k - f^\delta) \right), \quad (10)$$

for a neural network \mathcal{N} with parameters Ψ . Assuming the neural network is 1-Lipschitz, i.e.

$$\|\mathcal{N}_\Psi(u) - \mathcal{N}_\Psi(v)\| \leq \|u - v\|,$$

for all $u, v \in \mathbb{R}^n$ and choosing τ such that $\tau < 2/(\lambda \|K\|^2)$ is satisfied, then we observe that u^* with

$$u^* = \mathcal{N}_\Psi \left(u^* - \tau \lambda K^\top (K u^* - f^\delta) \right) \quad (11)$$

is a fixed point of iteration (10), which we can conclude from Banach's fixed point theorem if $K^\top K$ has full rank (in which case the fixed point is also unique); if $K^\top K$ does not have full rank, the mapping is only nonexpansive and non-emptiness of the fixed point set has to be verified (cf. [8]). Hence, we can guarantee convergence of the sequence. The Lipschitz continuity of the mapping $\mathcal{N}_\Psi(u - \tau\lambda K^\top(Ku - f^\delta))$ implies continuity, so we can characterize the fixed point via

$$\begin{aligned} u^* &= \lim_{k \rightarrow \infty} u^k = \lim_{k \rightarrow \infty} \mathcal{N}_\Psi(u^{k-1} - \tau\lambda K^\top(Ku^{k-1} - f^\delta)) \\ &= \mathcal{N}_\Psi\left(\lim_{k \rightarrow \infty} \left((I - \tau\lambda K^\top K)u^{k-1} + \tau\lambda K^\top f^\delta\right)\right) = \mathcal{N}_\Psi\left(\left((I - \tau\lambda K^\top K)u^* + \tau\lambda K^\top f^\delta\right)\right). \end{aligned}$$

This means that for the operator $G(u, \Psi) := \mathcal{N}_\Psi(u - \tau\lambda K^\top(Ku - f^\delta))$, the deep equilibrium problem (7) is well-defined if the conditions outlined above are met.

Another method that was considered in [12] is the so-called DeGrad-type method, which is motivated by gradient descent where a neural network is used to replace the gradient of a regularization term, i.e.

$$u^{k+1} = u^k - \tau \left(\lambda K^\top (Ku^k - f^\delta) + \mathcal{N}_\Psi(u^k) \right). \quad (12)$$

Making similar assumptions as in the DeProx case, we can assume that a (unique) fixed point exists, so that the deep equilibrium problem (7) is well-defined again.

2.3 Bilevel learning

Following the description of data-driven variational regularization models such as (6) in Section 2.1, we want to briefly recall how the parameters Ψ of the regularizer can be trained respectively identified with the help of bilevel learning. In this context, we can formulate the bilevel optimization problem as

$$\min_{\Psi} J(u^*), \quad (13a)$$

subject to

$$u^* \in \arg \min_u \left\{ \frac{\lambda}{2} \|Ku - f^\delta\|^2 + \mathcal{R}_\Psi(u) \right\}, \quad (13b)$$

where (13a) and (13b) are the upper-level and the lower-level problems, respectively. Here, J denotes a convex and continuously differentiable loss function, and $\mathcal{R}_\Psi : \mathbb{R}^n \rightarrow \mathbb{R} \cup \{\infty\}$ is a proper, convex and lower semi-continuous function that is parameterized by parameters Ψ . Note that due to the convexity of the lower-level problem, u^* will always be a global minimizer. Under suitable conditions on R (for example strong convexity), we can even conclude uniqueness of u^* . If the solution u^* is unique, its computation can also be replaced by a suitable fixed point iteration. To give an example, if \mathcal{R}_Ψ is considered differentiable, one can minimize the lower-level problem (13b) via an iterative strategy such as gradient descent, i.e.

$$u^{k+1} = u^k - \tau \left(\lambda K^\top (Ku^k - f^\delta) + \nabla \mathcal{R}_\Psi(u^k) \right), \quad (14)$$

for a sequence $\{u^k\}_{k=1}^\infty$ with arbitrary initial value u^0 and a positive step-size parameter τ . If τ is chosen appropriately, then convergence of (14) to u^* can be guaranteed. As a consequence, we can replace (13b) with the fixed point constraint

$$u^* = u^* - \tau \left(\lambda K^\top (Ku^* - f^\delta) + \nabla \mathcal{R}_\Psi(u^*) \right) \quad (15)$$

and therefore reformulate (13) to a saddle-point problem of the form of (8) with $G(u^*, \Psi) = u^* - \tau (\lambda K^\top (Ku^* - f^\delta) + \nabla \mathcal{R}_\Psi(u^*))$. Note that, depending on the choice of \mathcal{R}_Ψ , instead of gradient descent many other optimization algorithms can be chosen, which leads to a variety of different fixed point equations $u^* = G(u^*, \Psi)$ with the same fixed point u^* that can be chosen in (8).

2.4 Why naively learning fixed points does not work

We conclude this section by briefly addressing the problem of naively learning fixed points by minimizing empirical risks that measure the deviation between model output and desired output data u^\dagger . Suppose we choose the De-Prox architecture (10) from Section 2.2. Instead of solving (7) with G defined as $G(u, \Psi) = \mathcal{N}_\Psi(u - \tau \lambda K^\top (Ku - f^\delta))$ for $J(u) := \frac{1}{2} \|u - u^\dagger\|^2$, we could naively train the parameters Ψ by minimizing J defined as

$$J(u^\dagger) := \frac{1}{2} \left\| \mathcal{N}_\Psi \left(u^\dagger - \tau \lambda K^\top (Ku^\dagger - f^\delta) \right) - u^\dagger \right\|^2 \quad (16)$$

with respect to Ψ . Suppose $f^\delta = Ku^\dagger + \delta$, for some perturbation δ , then Problem (16) is the same as minimizing an empirical risk for a denoising autoencoder, i.e.

$$\min_{\Psi} \frac{1}{2} \left\| \mathcal{N}_\Psi \left(u^\dagger + \tau \lambda K^\top \delta \right) - u^\dagger \right\|^2. \quad (17)$$

The problem with (17) is that the network \mathcal{N}_Ψ is only trained to remove the term $\tau \lambda K^\top \delta$. However, if K is underdetermined (like in the inpainting application later), then \mathcal{N}_Ψ in iteration (10) also has to be able to combat any lack of information that stems from the underdeterminedness of K (for initial values other than u^\dagger). For that reason, solving (7) is superior over (17) in this particular context.

3 Architecture design and implementation

We compare deep equilibrium and bilevel learning methods empirically for three different inverse problems. In general, it is very difficult to have a fair comparison between different architectures, as their expressivity is not only determined by the number of parameters or the choice of activation functions, but the complex interplay of all architecture design choices as well as other factors like the optimization method that is used for training the models, or the choice of loss and regularization functions, to name only a few. We have therefore decided to choose two deep equilibrium models: one that belongs to the class of deep equilibrium proximal gradient descent models, cf. [21] and [12, Section 3.2], and one that belongs to the class of deep equilibrium gradient descent models, cf. [12, Section 3.1]. The latter we compare with a bilevel approach where the lower-level problem is computed via gradient descent, and both architectures are chosen to be as similar as possible. The individual models are described in detail in the following sections.

3.1 Deep equilibrium models

In this section we describe the specific deep equilibrium models that we use for the comparison of numerical results in Section 4. For a fairer comparison with bilevel optimization methods, we focus on models of type DeGrad as described in Section 2.2.

3.1.1 Deep equilibrium gradient descent

Following [12, Section 3.1], we define the deep equilibrium gradient descent method for the approximation of inverse problems solutions as

$$u^{k+1} = u^k - \tau \left(\lambda K^\top (Ku^k - f^\delta) + \mathcal{N}_\Psi(u^k) \right), \quad (18)$$

where $\mathcal{N}_\Psi : \mathbb{R}^n \rightarrow \mathbb{R}^n$ is a neural network with parameters Ψ . For the comparison with bilevel optimization methods, we will choose \mathcal{N}_Ψ as

$$\mathcal{N}_\Psi(u) = \gamma C^\top \sigma(Au + b), \quad (19)$$

for parameters $\Psi = (A, C, b)$ with matrices $A, C \in \mathbb{R}^{q \times r}$ and bias vector $b \in \mathbb{R}^q$, activation function $\sigma : \mathbb{R}^q \rightarrow \mathbb{R}^q$ and positive constant γ . Please note that (19) is not necessarily a gradient of a function with argument u , unless $C = A$ and suitable choices of σ . For consistency in the numerical examples below, we will choose the same activation functions discussed in Section 3.2.

3.2 Bilevel learning models

In order to effectively compare bilevel optimization with deep equilibrium models, we replace the solution of (13b) with the fixed point of (14). We choose $\mathcal{R}_\Psi(u)$ to be of the form

$$\mathcal{R}_\Psi(u) = \gamma \inf_v \left(\frac{1}{2} \|v - Au - b\|^2 + \mathcal{R}(v) \right), \quad (20)$$

which is the Moreau–Yosida regularization [22, 36] of the proper, convex and lower semi-continuous function $\mathcal{R} : \mathbb{R}^s \rightarrow \mathbb{R} \cup \{\infty\}$ composed with the affine-linear transformation $A \cdot + b$. Here $\Psi = (A, b)$ denote the model parameters, which are a matrix $A \in \mathbb{R}^{s \times n}$ and a bias vector $b \in \mathbb{R}^s$, and γ is a positive parameter. The gradient of \mathcal{R}_Ψ with respect to argument u reads

$$\nabla \mathcal{R}_\Psi(u) = \gamma A^\top (Au + b - \text{prox}_{\mathcal{R}}(Au + b)) = \gamma A^\top \text{prox}_{\mathcal{R}^*}(Au + b), \quad (21)$$

cf. [4, Proposition 12.30], where $\text{prox}_{\mathcal{R}} : \mathbb{R}^s \rightarrow \mathbb{R}^s$ denotes the proximal map [23] of \mathcal{R} , i.e.

$$\text{prox}_{\mathcal{R}}(w) = \arg \min_{v \in \mathbb{R}^s} \left\{ \frac{1}{2} \|v - w\|^2 + \mathcal{R}(v) \right\},$$

and $\text{prox}_{\mathcal{R}^*}$ denotes the proximal map of the convex conjugate \mathcal{R}^* of \mathcal{R} (cf. [5]) that is defined as

$$\mathcal{R}^*(p) := \sup_v (\langle v, p \rangle - \mathcal{R}(v)).$$

Note that (21) is equivalent to (19) if $C = A$ and if $\sigma = \text{prox}_{\mathcal{R}^*}$ for some proper, convex and lower semi-continuous \mathcal{R} with conjugate \mathcal{R}^* .

Suppose we define χ_C as the characteristic function over the convex set C , i.e.

$$\chi_C(u) := \begin{cases} 0 & u \in C \\ \infty & u \notin C \end{cases}.$$

If we choose $\mathcal{R}(u) = \chi_{C_1}(u)$ with $C_1 = \{0\}$, we observe $\mathcal{R}_\Psi(u) = \frac{1}{2}\|Au + b\|^2$ and $\mathcal{R}^*(p) = 0$. The proximal map of \mathcal{R}^* then simply reduces to the identity, i.e. $\text{prox}_{\mathcal{R}^*}(w) = w$, and (21) reduces to $\nabla \mathcal{R}_\Psi(u) = \gamma A^\top (Au + b)$.

Another interesting example is $\mathcal{R}(u) = \chi_{C_2}(u)$ with $C_2 = (-\infty, 0]^s$, where we recover the elementwise Rectified Linear Unit (ReLU) [24] activation function $\sigma(x) = \text{ReLU}(x)$ with

$$(\text{ReLU}(x))_i := \begin{cases} x_i & x_i \geq 0 \\ 0 & x_i < 0 \end{cases},$$

for the proximal map of the conjugate. In this case, (21) reduces to $\nabla \mathcal{R}_\Psi(u) = \gamma A^\top \text{ReLU}(Au + b)$.

If we choose $\mathcal{R}(v) = \varepsilon \|v\|_1 = \varepsilon \sum_{j=1}^m |v_j|$, we have $\mathcal{R}^*(p) = \chi_{C_3}(u)$ with $C_3 = \{u \mid \|u\|_\infty \leq \varepsilon\}$ and

$$\text{prox}_{\mathcal{R}^*}(w)_j = \begin{cases} \varepsilon & w_j > \varepsilon \\ w_j & |w_j| \leq \varepsilon \\ -\varepsilon & w_j < -\varepsilon \end{cases},$$

for all $j \in \{1, \dots, s\}$. Then (21) reduces to

$$(\nabla \mathcal{R}_\Psi(u))_j = \gamma \left(A^\top v \right)_j \quad \text{with} \quad v_i := \begin{cases} \varepsilon & (Au + b)_i > \varepsilon \\ (Au + b)_i & |(Au + b)_i| \leq \varepsilon \\ -\varepsilon & (Au + b)_i < -\varepsilon \end{cases},$$

for $i \in \{1, \dots, s\}$ and $j \in \{1, \dots, n\}$. If, in return, we choose $\mathcal{R}(u) = \chi_{C_3}(u)$, we recover the elementwise soft-shrinkage activation function $\text{prox}_{\mathcal{R}^*}(x) = \text{Softshrink}_\varepsilon(x)$ with

$$(\text{Softshrink}_\varepsilon(x))_i := \begin{cases} x_i + \varepsilon & x_i < -\varepsilon \\ 0 & |x_i| \leq \varepsilon \\ x_i - \varepsilon & x_i > \varepsilon \end{cases},$$

in which case (21) reduces to $\nabla \mathcal{R}_\Psi(u) = \gamma A^\top \text{Softshrink}_\varepsilon(Au)$.

3.3 Inverse problems

We compare deep equilibrium and bilevel learning for the three different inverse problems of denoising, inpainting and deblurring, which we briefly describe in the following subsections.

3.3.1 Denoising

In the denoising task we assume measured data f is affected by additive noise δ only. This means that $K = I_n$, where $I_n \in \{0, 1\}^{n \times n}$ is the identity matrix of size n , so equation (1) reads

$$u + \delta = y^\delta.$$

It is also clear that u and f have the same dimension in this setting. The main goal is to remove the noise δ to retrieve x from y .

3.3.2 Inpainting

In (image) inpainting we have a partial observation f of unknown, complete data u . For example, an image can have missing pixels when a user may want to remove an undesired object from said image. The task of filling missing pixels is called inpainting, and it can be modeled as an inverse problem [31]. The matrix K can be modeled by removing every row that corresponds to a missing pixel from an identity matrix I_n . If we want u and f^δ to have the same dimension (i.e. $m = n$), it suffices to substitute zero instead of one in each row that corresponds to a missing pixel.

3.3.3 Deblurring

In (image) deblurring the goal is to recover an unknown image u from a blurred and usually noisy image f^δ . This process can mathematically be described with the inversion of a convolution operator, which without regularization is highly ill-conditioned. We consider images as flattened vectors $u \in \mathbb{R}^n$. If we want to apply convolutions to images, we can consider $U \in \mathbb{R}^{n_{\text{row}} \times n_{\text{col}}}$, where $n_{\text{row}} \times n_{\text{col}} = n$, and $n_{\text{row}}, n_{\text{col}} \in \mathbb{N}$, and consider u as the flattened version of U .

A two-dimensional convolution operator K_Ω is then defined as $K_\Omega U = F_{\text{img}}^\delta$, with $[F_{\text{img}}^\delta]_{h,k} = \sum_{i=-a}^a \sum_{j=-b}^b [\Omega]_{i,j} [U]_{h-i, k-j}$ for all h, k , where Ω is a fixed *convolution kernel*. The components of Ω are usually normalized to guarantee $\sum_i \sum_j [\Omega]_{i,j} = 1$.

3.4 Implementation

For the bilevel learning, we want to obtain the fixed point solution u^* defined in (15). We do this by initializing u_0 as the zero vector without loss of generality, and then we iteratively use (14). Note that any initial value for u_0 can be chosen because of convergence guarantees to the unique fixed point u^* . We accelerate the convergence towards the fixed point solution by using Anderson acceleration [34] following the approach and the parameters chosen in [12]. This means that Anderson acceleration is computed until at least one of two stopping conditions is satisfied: either the tolerance $u^k - u^{k-1}$ is below a threshold, or the maximum number of iterations is reached. We choose 10^{-3} as threshold, and 50 as maximum number of iterations because we experimentally discover that we can get a good trade-off between the quality of the reconstructed image and the computation time with this setting.

For deep equilibrium regularizers, we solve (18), where \mathcal{N}_Ψ works as a parametrized regularizer defined in (19). This means that the neural network we are using is composed of one fully-connected affine input layer with activation function σ , and one output layer with no bias nor activation function, scaled by a scalar γ which we consider as a hyperparameter chosen a-priori (i.e. it is not trained).

For bilevel learning models, we use the same setting with the additional constraint $C = A$ for the reasons explained in Section 3.2.

The chosen optimizer for training parameters Ψ is Adam [16] with batch size 100, and initial learning rate 10^{-3} , used in combination with a cosine annealing schedule with $\eta_{\min} = 10^{-6}$ and T_{\max} equal to the product of the batch size times the number of expected epochs (i.e. respectively 100 and 100).

4 Numerical results

We compare bilevel optimization method and deep equilibrium model in our numerical experiments. In particular, we want to experimentally verify whether one method works better than the other. The model used for the bilevel optimization examples is defined in (14). For deep equilibrium models, we use (18)-(19).

We use the MNIST dataset [20], a dataset of digits that contains 70,000 grayscale images (60,000 for training, and 10,000 testing). Each image has size 28×28 , which are flattened and used as row vectors. We rescale pixel values so that they are within the range $[-1, 1]$. Those images are the unknown u we want to retrieve in (3). To generate the input f^δ , operator K (either denoising, inpainting, or deblurring described in Section 3.3) is applied to u . To avoid committing an inverse crime, instances δ of Gaussian random variables are added, where $\delta_i \sim \mathcal{N}(0, \alpha^2)$, and α is the noise level hyperparameter. We use $\alpha = 0.0, 0.05, 0.1, 0.5, 1.0$ for noise levels in training, and we keep the same value of α for the test dataset. We note that instances δ of Gaussian random variables are not generated once for each image; instead we generate new values of δ at each training epoch.

For the regularizers, we show numerical results for the identity, ReLU and Softshrink activation functions. The hyperparameters are set to the values $\tau = 0.01, 0.1, 0.9, 1.1, 2.1$, and $\gamma = 0.1, 0.5, 1.0$. We initialize A and C as square matrices with dimension 784×784 . It follows that the bias b has dimension 784. This is not the only possible choice, since it is sufficient that A and C have the same dimension (i.e. they can be rectangular matrices). We choose to initialize the activation function σ as (*ReLU*), (*Softshrink*), or (*identity*), as discussed in Section 3.2. The value for the threshold of the (*Softshrink*) activation function is chosen as τ , although in principle they are different parameters and they can be chosen differently.

We choose the mean-squared error (MSE) as the loss function to minimize the euclidean distance between the original MNIST images u and the reconstructed images u^* .

The simulations are coded using Python (v3.8.5), and in particular the PyTorch (v1.10) library. All the simulations run on the CPU and not on the GPU for reproducibility purposes (the GPU introduces some non-deterministic behaviors), although the code can be easily run on a GPU, with remarkable speed-up in terms of computation time. The code has been written and tested on a local Windows 10 laptop, and the simulations were run on the High Performance Cluster system Apocrita [15]. The code for will be available and can be used under the Creative Commons Attribution (CC BY) license once the article is accepted for publication.

4.1 Denoising

We start analyzing the denoising task. As it can be expected, our experiments suggest that the denoising task is the easiest among the three tasks considered. Indeed, we see from Fig.1 that the average loss of the trained model is lower in the denoising task, and the interquantile range is smaller too.

The visual comparison between bilevel optimization method and deep equilibrium model is shown in Fig.2. The original image (without noise) can be recovered by both methods, and there are no major differences between the reconstructions of the two methods. All the models that achieve a loss smaller than 0.5 achieve similar visual results.

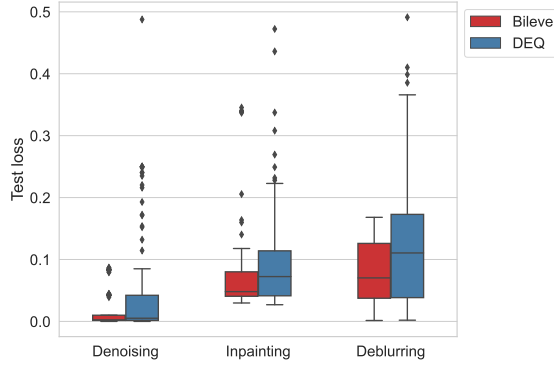


Figure 1: Comparison between bilevel optimization and deep equilibrium models for each of the three considered inverse problems, namely denoising, inpainting, and deblurring, over all the range of possible parameters. These boxplots consider the loss of the trained models evaluated on the test dataset. We removed all the configurations with a final loss larger than 0.5, a value we arbitrarily chose by looking for an empirical relation between the loss and the image quality.

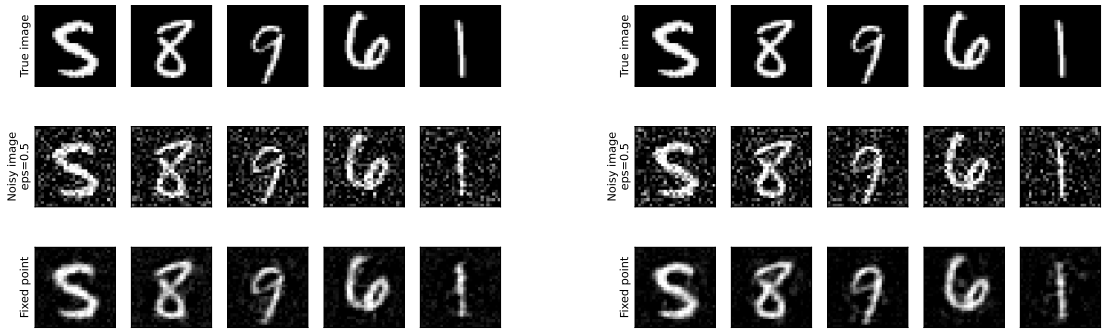


Figure 2: Denoising the MNIST dataset. Visual comparison between bilevel method (left) and deep equilibrium model (right), with parameters $\tau = 0.5$, $\gamma = 0.1$, and $\sigma = (\text{ReLU})$. Images are taken from the test dataset. The first row shows the original images; the second row is the model input. The last row is the output of the trained models.

4.2 Inpainting

For inpainting, we choose to mask one third of the image rows, starting from the top and rounding up to the nearest integer. For MNIST images, this corresponds to masking 10 rows out of 28. Note that this task is harder than recovering the same number of pixels if they were randomly selected. In this latter scenario, the values of each missing pixel can be reasonably guessed by looking at the values of its neighbors, which is not true in our setting because most of the missing pixels are surrounded by other missing pixels. Only 117 hyperparameter-settings out of 225 worked for the bilevel model. Deep equilibrium models are more sensitive to the hyperparameter selection than bilevel methods for the inpainting task, since only 73 hyperparameters settings out of 225 lead to satisfactory results. We see from Fig.1 that the chosen bilevel methods seem to perform better than their deep equilibrium counterparts in

terms of loss minimization.

Visual results are shown in Fig.3. Interestingly, both methods achieve good images reconstructions.

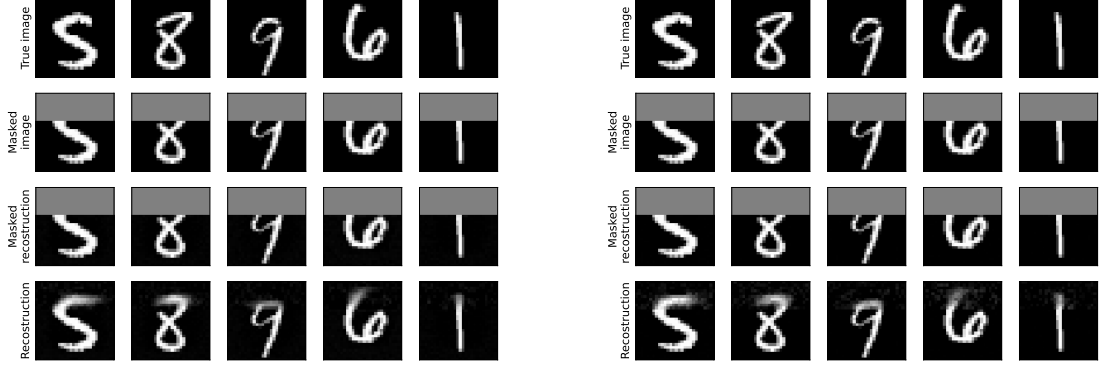


Figure 3: Inpainting MNIST. Comparison between bilevel method (left) and deep equilibrium model (right), with parameters $\tau = 0.5$, $\gamma = 1.0$, and $\sigma = (\text{Softshrink})$. Images are taken from the test dataset. The first row shows the original image, the second row is the masked image, i.e. the input of the algorithm. The fourth row is the output of the trained models. Finally, the third row shows what happens when we apply the inpainting operator on the output. The fourth row is the output of the trained deep equilibrium optimization problem. Ideally, the difference between the second and third row should be small.

4.3 Deblurring

The last task we consider is deblurring. We model the convolution operator to mimic a diagonal motion blur, for which we choose the convolution kernel Ω as $\Omega = \frac{1}{5}I_5$, where I_5 denotes the 5×5 identity matrix. This task has the largest variability in terms of loss results for trained models, as shown in Fig.1. We also see that bilevel methods achieve a smaller average loss in comparison to deep equilibrium models, with also a smaller interquantile range. The quality of the retrieved images is similar for the two methods as shown in Fig.4, even though the average loss seems to suggest a different result (this is because the mean-squared error is not always a good indicator of *similarity* between a pair of images).

4.4 Sensitivity against noise level

The number of parameters in deep equilibrium models is larger than the one for bilevel methods in the framework we considered. Therefore, we want to assess whether this has an impact on the loss for different noise levels. To do so, we visualize the loss for both training and test datasets. Results are shown in Fig.5. Both methods seem to have the same behavior for increasing noise level values. Training takes longer for larger noise levels, and the loss becomes larger and larger as expected.

4.5 Sensitivity against hyperparameter selection

Deep equilibrium models have twice as many parameters as bilevel learning methods in our setting. For our computations, we capped the running time to at most one hour, which is

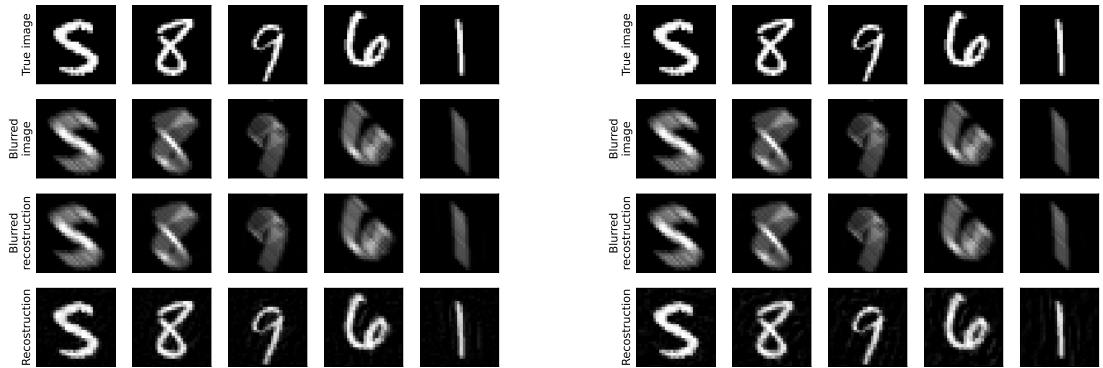


Figure 4: Deblurring MNIST. Comparison between bilevel method (left) and deep equilibrium model (right), with parameters $\tau = 0.5$, $\gamma = 0.5$, and $\sigma = (\text{Softshrink})$. Images are taken from the test dataset. The first row shows the original images; the second row is the model input. The last row is the output of the trained models. The third row shows the model output after we apply the convolution kernel to it. Ideally, the difference between the second and the third rows should be small.

why we need to evaluate the impact of this choice on the results. To do so, we consider all the simulations, keeping only those with a final test loss smaller than 0.5, and collect the number of epochs in bins in a histogram. The resulting histograms are shown in Fig.6. The shapes of bilevel and deep equilibrium histograms are similar, suggesting that capping the running time to one hour for the simulations does not have an impact on the quality of the results. The different scale of the y axes for the two plots reflects that more simulations for the deep equilibrium models have exceeded the loss threshold of 0.5 in comparison to the bilevel methods. This further supports that the chosen bilevel methods are less sensitive to hyperparameter selection than their deep equilibrium counterparts.

5 Conclusions & Outlook

We have framed bilevel learning methods as deep equilibrium methods and have compared several models of each class of similar complexity with each other. From those numerical results, we have observed that the two methods behave similarly in terms of average loss when they are used as regularizers. We can even argue that regularizers trained by bilevel learning were performing slightly better than their deep equilibrium counterparts, which can have different reasons. The average loss of the trained models with bilevel learning is smaller, with a lower interquantile range than deep equilibrium models. The results also suggest bilevel learning is less sensitive to the choice of hyperparameters than deep equilibrium method, making it more robust in terms of hyperparameters selection, and easier to train. This is in contrast to the a-priori assumption that deep equilibrium models might perform better because they are more general than their bilevel learning counterparts. The number of parameters in the deep equilibrium models we considered is around twice than the ones of the bilevel learning models. It would be reasonable to assume that the former might perform better than the latter in terms of minimizing the loss function, due to a greater number of degrees of freedom in terms of parameter choice. However, this is not what we experienced in our experiments. We emphasize that these observations are limited to the gradient descent deep equilibrium

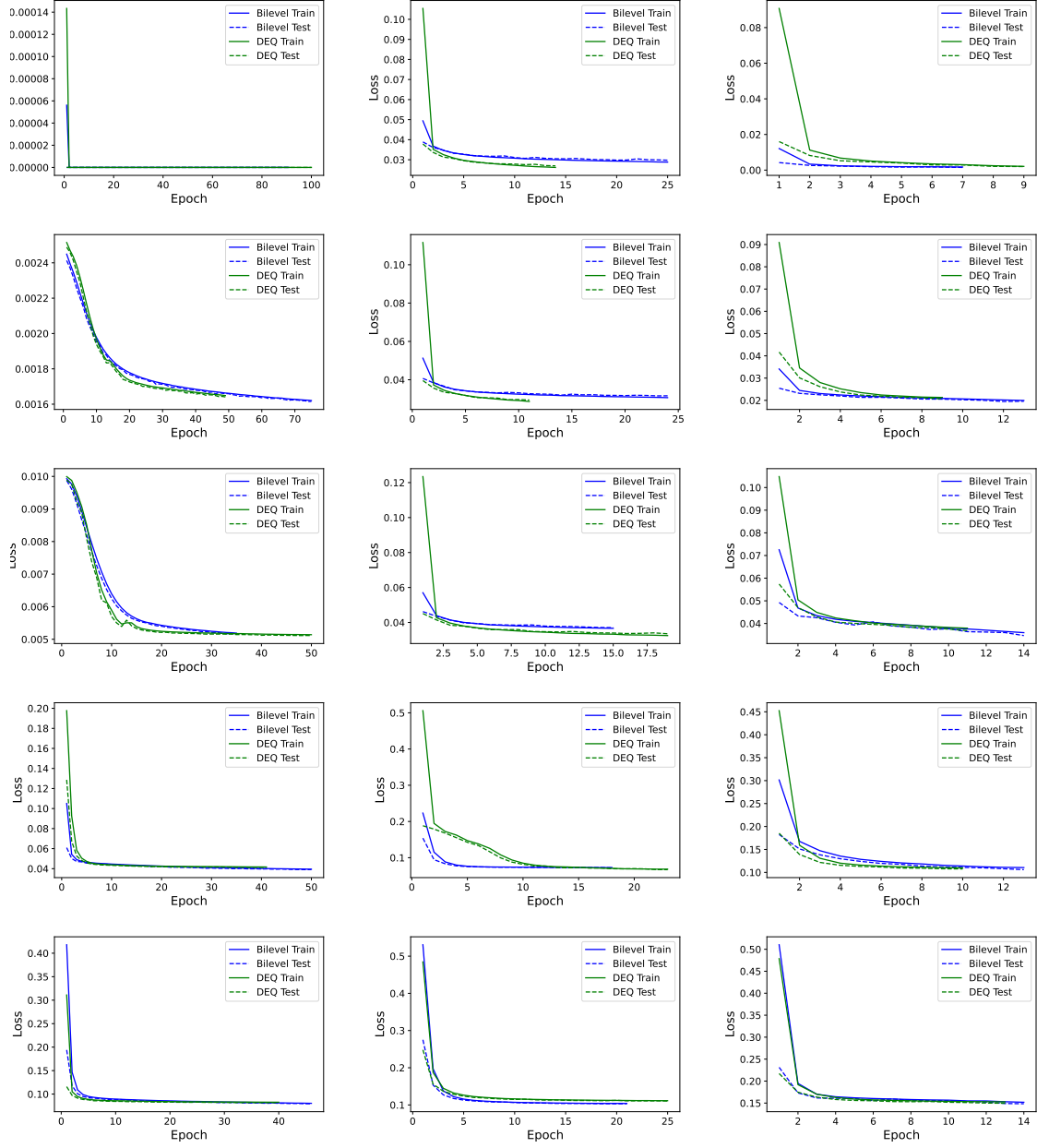


Figure 5: Comparison of the loss error for the test dataset evaluated after each training epoch, for increasing values of noise levels in training (noise levels from top to bottom row: 0, 0.05, 0.1, 0.5, 1). Simulations are grouped by the tasks, namely denoising, inpainting, and deblurring (left, center, right columns). Each plot shows the simulation with the configurations that achieve the lowest final test loss.

architecture. Further comparisons with other deep equilibrium architectures are subject to future work. It would also be interesting to study deep equilibrium models mathematically in greater detail, and to identify conditions that can lead to theoretical guarantees for them.

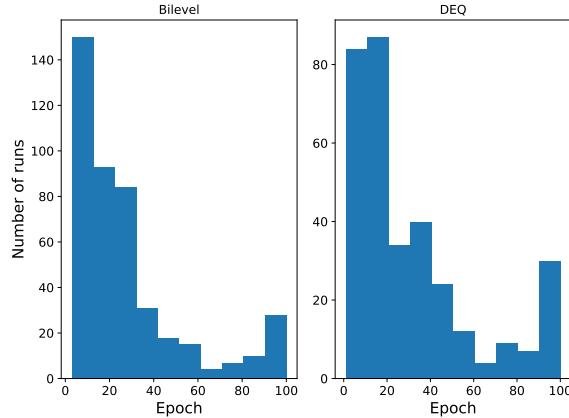


Figure 6: These histograms show how many simulations were finished within an hour as a function of the number of epochs. Each simulation is a different configuration of hyperparameters. We consider only those runs where the loss on the test dataset is smaller than 0.5.

Acknowledgements

The authors would like to thank the Isaac Newton Institute for Mathematical Sciences, Cambridge, for support and hospitality during the programme *Mathematics of Deep Learning* where work on this paper was undertaken. This work was supported by EPSRC grant no EP/R014604/1. This research utilized Queen Mary’s Apocrita and Andrena HPC facilities, supported by QMUL Research-IT <http://doi.org/10.5281/zenodo.438045>. DR acknowledges support from EPSRC grant EP/513106/1. MJE acknowledges support from the EPSRC (EP/S026045/1, EP/T026693/1, EP/V026259/1) and the Leverhulme Trust (ECF-2019-478).

References

- [1] Jonas Adler and Ozan Öktem. “Learned Primal-Dual Reconstruction”. In: *IEEE Transactions on Medical Imaging* 37 (6 2018), pp. 1322–1332.
- [2] Jonas Adler and Ozan Öktem. “Solving ill-posed inverse problems using iterative deep neural networks”. In: *Inverse Problems* 33 (2017), p. 124007.
- [3] Shaojie Bai, J Zico Kolter, and Vladlen Koltun. “Deep Equilibrium Models”. In: *Advances in Neural Information Processing Systems* 32. 2019.
- [4] Heinz H Bauschke, Patrick L Combettes, et al. *Convex analysis and monotone operator theory in Hilbert spaces*. Vol. 408. Springer, 2011.
- [5] Amir Beck. *First-order methods in optimization*. SIAM, 2017.
- [6] Martin Benning and Martin Burger. “Modern regularization methods for inverse problems”. In: *Acta Numerica* 27 (2018), pp. 1–111.
- [7] Yunjin Chen, Rene Ranftl, and Thomas Pock. “Insights into analysis operator learning: From patch-based sparse models to higher order MRFs”. In: *IEEE Transactions on Image Processing* 23.3 (2014), pp. 1060–1072.

- [8] Patrick L Combettes and Jean-Christophe Pesquet. “Fixed point strategies in data science”. In: *IEEE Transactions on Signal Processing* 69 (2021), pp. 3878–3905.
- [9] Caroline Crockett and Jeffrey A. Fessler. *Bilevel Methods for Image Reconstruction*. 2021. URL: <http://arxiv.org/abs/2109.09610>.
- [10] Matthias J. Ehrhardt and Lindon Roberts. “Inexact Derivative-Free Optimization for Bilevel Learning”. In: *Journal of Mathematical Imaging and Vision* 63 (5 2021), pp. 580–600.
- [11] Heinz Werner Engl, Martin Hanke, and Andreas Neubauer. *Regularization of inverse problems*. Vol. 375. Springer Science & Business Media, 1996.
- [12] Davis Gilton, Greg Ongie, and Rebecca Willett. “Deep Equilibrium Architectures for Inverse Problems in Imaging”. In: *IEEE Transactions on Computational Imaging* (2021).
- [13] Karol Gregor and Yann LeCun. “Learning Fast Approximations of Sparse Coding”. In: *27th International Conference on Machine Learning*. 2010, pp. 399–406.
- [14] Kyong Hwan Jin et al. “Deep Convolutional Neural Network for Inverse Problems in Imaging”. In: *IEEE Transactions on Image Processing* 26 (9 Sept. 2017), pp. 4509–4522. ISSN: 10577149.
- [15] Thomas King, Simon Butcher, and Lukasz Zalewski. *Apocrita - High Performance Computing Cluster for Queen Mary University of London*. Mar. 2017. URL: <https://doi.org/10.5281/zenodo.438045>.
- [16] Diederik P Kingma and Jimmy Ba. “Adam: A method for stochastic optimization”. In: *arXiv preprint arXiv:1412.6980* (2014).
- [17] Erich Kobler et al. “Total Deep Variation: A Stable Regularizer for Inverse Problems”. In: *accepted by IEEE Transactions on Pattern Analysis and Machine Intelligence* (2020).
- [18] Erich Kobler et al. “Variational networks: Connecting variational methods and deep learning”. In: *Lecture Notes in Computer Science (including subseries Lecture Notes in Artificial Intelligence and Lecture Notes in Bioinformatics)* 10496 LNCS (2017), pp. 281–293.
- [19] Karl Kunisch and Thomas Pock. “A Bilevel Optimization Approach for Parameter Learning in Variational Models”. In: *SIAM Journal on Imaging Sciences* 6 (2 2013), pp. 938–983.
- [20] Yann LeCun, Corinna Cortes, and Christopher J.C. Burges. *MNIST handwritten digit database*. 1998. URL: <http://yann.lecun.com/exdb/mnist/>.
- [21] Morteza Mardani et al. “Neural proximal gradient descent for compressive imaging”. In: *Advances in Neural Information Processing Systems* 31 (2018).
- [22] Jean Jacques Moreau. “Fonctions convexes duales et points proximaux dans un espace hilbertien”. In: *Comptes rendus hebdomadaires des séances de l’Académie des sciences* 255 (1962), pp. 2897–2899.
- [23] Jean-Jacques Moreau. “Proximité et dualité dans un espace hilbertien”. In: *Bulletin de la Société mathématique de France* 93 (1965), pp. 273–299.
- [24] Vinod Nair and Geoffrey E Hinton. “Rectified linear units improve restricted boltzmann machines”. In: *ICML*. 2010.

- [25] Frank Natterer and Frank Wübbeling. *Mathematical methods in image reconstruction*. SIAM, 2001.
- [26] Peter Ochs et al. “Bilevel Optimization with Nonsmooth Lower Level Problems”. In: *SSVM*. Vol. 9087. 2015, pp. 654–665.
- [27] J. C. De los Reyes, Carola-Bibiane Schönlieb, and T. Valkonen. “Bilevel Parameter Learning for Higher-Order Total Variation Regularisation Models”. In: *Journal of Mathematical Imaging and Vision* 57 (1 2017), pp. 1–25.
- [28] Juan Carlos De Los Reyes and Carola-Bibiane Schönlieb. “Image Denoising: Learning the Noise Model via Nonsmooth PDE-Constrained Optimization”. In: *Inverse Problems and Imaging* 7 (2013), pp. 1183–1214.
- [29] Stefan Roth and Michael J Black. “Fields of experts”. In: *International Journal of Computer Vision* 82.2 (2009), pp. 205–229.
- [30] Otmar Scherzer et al. *Variational methods in imaging*. Springer, 2009.
- [31] Carola-Bibiane Schönlieb. *Partial differential equation methods for image inpainting*. Vol. 29. Cambridge University Press, 2015.
- [32] A.N. Tikhonov, A. Goncharsky, and M. Bloch. “Ill-posed problems in the natural sciences”. In: *Mir* (1987).
- [33] Andrei Nikolaevich Tikhonov. “On the solution of ill-posed problems and the method of regularization”. In: *Doklady Akademii Nauk*. Vol. 151. 3. Russian Academy of Sciences. 1963, pp. 501–504.
- [34] Homer F. Walker and Peng Ni. “Anderson Acceleration for Fixed-Point Iterations”. In: *SIAM Journal on Numerical Analysis* 49.4 (2011), pp. 1715–1735.
- [35] Guang Yang et al. “DAGAN: Deep De-Aliasing Generative Adversarial Networks for Fast Compressed Sensing MRI Reconstruction”. In: *IEEE Transactions on Medical Imaging* 37 (6 2018), pp. 1310–1321.
- [36] Kōsaku Yosida. *Functional analysis*. Springer, 1964.
- [37] Bo Zhu et al. “Image Reconstruction by Domain-Transform Manifold Learning”. In: *Nature* 555 (7697 2018), pp. 487–492.